A New Gas-Content-Evaluation Method for Organic-Rich Shale Using the Fractionation of Carbon Isotopes of Methane

Gaohui Cao, Institute of Mechanics, Chinese Academy of Sciences, and School of Engineering Science, University of Chinese Academy of Sciences; **Huanxu Zhang,** College of Engineering, Peking University, and Shandong Provincial Key Laboratory of Depositional Mineralization and Sedimentary Minerals, Shandong University of Science and Technology; **Wenbin Jiang,** Institute of Mechanics, Chinese Academy of Sciences; **Sheng Wu,** Power Environmental Energy Research Institute; **Di Zhu*,** Energy Research Institute, Qilu University of Technology (Shandong Academy of Science); and **Mian Lin**,** Institute of Mechanics, Chinese Academy of Sciences, and School of Engineering Science, University of Chinese Academy of Sciences

Summary

Gas content is a key parameter for the determination of the gas resources in unconventional reservoirs. In this study, we propose a novel method to evaluate the gas content of shale through a new perspective: fractionation of carbon isotopes of methane. At first, a bicomponent gas-convection/diffusion/adsorption model (BG-CDAM) is successfully built with consideration of the flow and adsorption difference between $^{13}CH_4$ and $^{12}CH_4$ in the nanoporous shale. A detailed understanding of the mechanism of fractionation of the isotopes is obtained for the first time and the Knudsen-diffusivity difference is identified as the dominant factor for fractionation according to the different molecular weights of the isotopes. Then, the simulated results of BG-CDAM and the measured data from an isotope-logging test are combined to determine the unknown parameters for gas-content calculation. The proposed method for organic shale is valid and useful to obtain the quantitative component proportion in gas content, such as lost gas, degassing gas and residual gas, or free gas and adsorption gas. Thus, this method could provide a promising means for the identification of sweet spots in shale-gas reservoirs. Moreover, the method might have the potential to economically and rapidly evaluate the remaining resources in producing wells in future applications.

Introduction

Shale gas is the natural gas retained and accumulated in source shale and it is characterized as self-generating and self-storing. It is mainly stored in shale reservoirs in the forms of free gas and adsorption gas. Adsorption gas, with proportion ranges from 20 to 85% (average of 50%) of the total gas in shale (Curtis 2002; Zhang et al. 2004), has a close relationship with the gas content (Meng et al. 2016). Although there might be a wide range of gas content in organic-shale formations, only when gas content reaches a certain level (for example, the gas-content limit in the US is 0.5 to $1.0\,m^3/t$) can it be considered economical to develop (Zhang et al. 2012). The exploration and development of shale gas have attracted extensive attention around the world. For shale-gas exploration, the search and evaluation of sweet spots have always been the primary consideration. Gas content plays an important role in the identification of sweet spots.

Over the past few decades, several methods, including both indirect and direct methods, have been established for the evaluation of shale- and coalbed-gas content. Indirect methods generally involve estimating free-gas content from well-logging measurements and estimating the adsorbed-gas content from adsorption isotherms in the laboratory (Dang et al. 2017). The free-gas amount is dependent on the measurements of porosity and saturation, whereas the amount of adsorbed gas is obtained by high-pressure methane-isotherm adsorption. Therefore, gas content in shale can be calculated by summing the adsorbed- and free-gas contents. Unlike indirect methods, direct methods measure the amount of gas actually released from shale samples and are often preferred because of their reliable and precise gas-degassing data. It is worth noting that to avoid confusion, in this paper, the expulsion of methane from the shale rock is referred as "degassing," and the release of methane from the pore surface is referred as "desorption." Direct methods include the US Bureau of Mines (USBM) method (Diamond et al. 1985; Pillalamarry et al. 2011), the Smith and Williams (1981, 1984) method, the Amoco curve-fit (ACF) method (Dan et al. 1993), and the modified-curve-fit (MCF) method (Yuan et al. 2014). These direct methods generally involve a three-step process. First, shale samples are retrieved and sealed in a degassing canister. The amount of the released gas replaced by water is designated as "degassed gas." Second, the "residual gas" is determined by collecting the released gas after grinding the core samples. The third step is to estimate the "lost gas" from the gas-degassing data using different methods (Dang et al. 2017). For example, the USBM method considers the degassing of gas from cores as a diffusion process by spherical particles with a constant initial gas concentration and a surface concentration of zero. The method uses some early degassing data to estimate the lost-gas content. The ACF method is different from the USBM method, in that it uses only the partial degassing data, by fitting all the gas-degassing data to obtain the lost gas. Yuan et al. (2014) noted that both the USBM and ACF methods apply the "unipore" model, which is inadequate to describe the gas-releasing process of organic-rich shale that has a heterogeneous pore-size distribution over the entire time. They proposed a new method, MCF, that uses a "bidisperse" diffusion model of macropores and micropores to fit all degassing data. However, the USBM, ACF, and MCF methods do not consider that the diffusivity varies with pressure through the degassing process, which will induce errors because many studies have shown obvious non-Darcy effects in gas transport in shale (Javadpour 2009; Civan et al. 2010; Darabi et al. 2012). In addition, many researchers noted that the lost gas is the most unreliable part of the total gas

---

* Corresponding author; email: zhud@sderi.cn

** Corresponding author; email: linmian@imech.ac.cn

content in the existing methods (Dang et al. 2017). The method for residual gas content is also imprecise. Since 2008, many researchers from different institutions and universities in China have performed many assessments for shale-gas resources. In many exploited gas wells, the shale-gas-content evaluations apply the conventional gas-degassing methods and equipment used for coalbed gas. The USBM direct method is most used in the estimation for the lost gas of shale (Dang et al. 2017). Although many scholars have proposed some improvement and optimization methods for gas-content measurements (Liu et al. 2010; Ying et al. 2011; Hu et al. 2014), it is still difficult to obtain an accurate lost-gas amount. Whether the USBM method is applicable to Chinese shale gas is still in doubt (Yao et al. 2016).

So far, the carbon-isotope composition of gas is widely used in hydrocarbon exploration to determine the composition and thermal maturity of source rocks (Feng et al. 2016; Wei et al. 2016; Zhang et al. 2018). Golding et al. (2013) summarized the studies of stable-isotope geochemistry of coalbed and shale gas and related production waters and noted that detailed studies about the stable isotope are essential to determine their gas origins and dominant methanogenic pathway. The analyses of Australian coal and marine-shale samples indicate that during gas desorption, both molecular and isotopic compositions change with time, yet many published classification systems relating the isotope composition of gas to source rock and thermal maturity do not consider the effects of such isotope fractionation (Faiz et al. 2018). Therefore, a detailed understanding of the mechanism of isotope fractionation is required to improve our ability to characterize source rocks and fluids. However, the research on carbon-isotope fractionation of methane is far from complete. Cui et al. (2009) and Yi et al. (2009) considered the fractionation caused by the different transitions between the adsorbate phase and the free-gas phase of $^{13}CH_4$ and $^{12}CH_4$. However, instead of adsorption, Zhang and Krooss (2001), Schloemer and Krooss (2004), and Richter et al. (2006) described isotope fractionation caused by gas migration considering pure-diffusion models. By coupling adsorption/desorption and diffusion, Xia and Tang (2012) built a continuum flow model to describe the isotope fractionation of natural gas in low-permeability rocks. The results strongly suggest that isotope fractionation in adsorption/desorption systems is dominated by mass transport rather than by the fractionation between the adsorbate phase and the free-gas phase. They also found that stronger adsorption affinity and larger adsorption capability result in much more negative isotopic composition of early gas from sources, and adsorption will affect the overall mass transport of methane. However, the discussed studies also have some deficiencies because they do not distinguish different flow mechanisms in the transport process, and the diffusivities of $^{13}CH_4$ and $^{12}CH_4$ are generally regarded as constant. On the basis of isotope experiments, Meng et al. (2016) studied the variation of carbon-isotope composition of alkane during the degassing process of shale gas using shale samples from the Chang 7 continental shale of the Yanchang Formation, China. Their results show that the carbon-isotope composition of methane increases during shale-gas degassing. Qin et al. (2017) also found that the carbon-isotope composition of methane becomes heavier with the degassing time through experiments using Longmaxi Shale of the Jiaoshiba area in Sichuan Basin, China. They noted that the fractionation might be mainly caused by adsorption/desorption and the diffusion of isotopes but have not given a detailed quantitative analysis. Moreover, whether the dominant factor for fractionation is adsorption/desorption or diffusion is still in debate.

In summary, as for the assessment of gas content in shale, most of the current methods follow the treatment of coalbed methane. However, there are many differences between shale gas and coalbed methane, including burial depth. In addition, most of the producing shale-gas reservoirs in China are deeply buried, with some reservoirs reaching between 3000 and 5000 m. Therefore, the lost gas is important. However, the calculation of lost gas using the current gas-degassing methods and equipment used for coalbed gas is doubtful. A more-precise method for gas content is urgently needed. The isotopic composition of methane is a refined value and is widely used in the geochemical field, and can provide a more-precise calculation method for gas content. However, whether the fractionation of carbon isotopes of methane is caused by diffusion action, adsorption/desorption action, or their combined action is still unknown (Qin et al. 2017). Here, the key problem is which process could first generate methane with a light isotopic composition and then become heavier. The main objective of this study is to identify the dominant factor for fractionation and then combine the measured data in an isotope-logging test and simulations to obtain the gas content for shale.

In this study, we build a BG-CDAM considering viscous flow, Knudsen diffusion, and the competitive adsorption of $^{13}CH_4$ and $^{12}CH_4$. Because of the strong heterogeneity between organic matter (OM) and inorganic matter (IOM) in shale, treating them separately has become a recognized idea in recent years (Naraghi and Javadpour 2015; Cao et al. 2018). In this model, OM and IOM are also distinguished by their different pore sizes, porosity, and adsorption. The percentages of OM and IOM are given by the volumetric total organic carbon (TOC) from well logging, and their spatial distributions are simplified as the sample sizes reach the organic representative-elementary-volume scale (Cao et al. 2018). Using the BG-CDAM, the influences of different flow mechanisms on isotope fractionation are analyzed. Then, the simulated results of BG-CDAM and the measured data from isotope logging are matched to determine the unknown parameters in gas-content calculations. On the basis of these parameters, we calculate the gas content of shale, and the percentages of the lost gas, degassing gas and residual gas (or free gas and adsorption gas) are also obtained. After determining the gas contents of the shale samples from different formations of Well DY5 in the Dingshan District, Chongqing, China, the corresponding sweet spots are also identified.

Model Establishment

BG-CDAM. In this study, we build a BG-CDAM by considering viscous flow, Knudsen diffusion, and the competitive adsorption of $^{13}CH_4$ and $^{12}CH_4$, as shown in **Fig. 1**. In BG-CDAM, shale samples are modeled as symmetrical regular spheres in which OM is surrounded by IOM. At the initial condition, high-pressure isotopic gases are stored in the samples and then released into the container. Some assumptions in establishing the model include the following:

1. The temperature is constant.
2. The shale samples consist of uniform regular spheres.
3. The pore shapes in the model are cylindrical tortuous tubes.
4. Shale gas is composed of $^{13}CH_4$ and $^{12}CH_4$, and other gas components such as C_{2-5} are ignored.
5. Adsorption in IOM is negligible. We assign adsorption only in OM.

Considering the different properties in OM and IOM, their treatments are varied.

First, according to the principle of conservation of mass considering Knudsen diffusion and viscous flow, the equation for IOM is

$$
\begin{cases}
\dfrac{V\phi_{e,\text{IOM}}}{RT}\dfrac{\partial p_1}{\partial t} = -\iiint\limits_V \nabla \vec{N}_1 \, dV \\[2em]
\dfrac{V\phi_{e,\text{IOM}}}{RT}\dfrac{\partial p_2}{\partial t} = -\iiint\limits_V \nabla \vec{N}_2 \, dV,
\end{cases}
\quad \dots \dots \dots \dots \dots \dots \dots \dots \dots \dots \dots \dots \dots \dots \dots \dots \dots \quad (1)
$$

where $\phi_{e,\text{IOM}}$ is the effective porosity of OM, V is the control volume, p_i is the partial pressure of the gas component i ($i = 1$ for $^{13}\text{CH}_4$, $i = 2$ for $^{12}\text{CH}_4$), R is the universal gas constant, T is absolute temperature (in K), and N_i is the mass flux of gas component i considering viscous flow and Knudsen diffusion, which will be described in detail later.
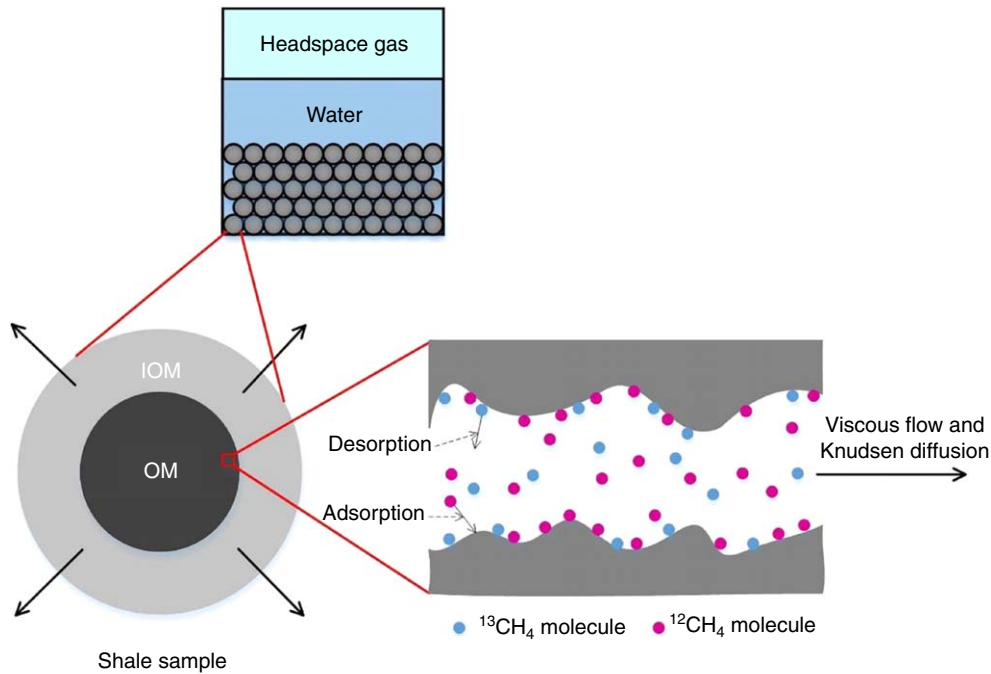

Fig. 1—Schematic of BG-CDAM.

Second, regarding OM, considering viscous flow, Knudsen diffusion, and competitive adsorption, the conservation equation takes the form

$$
\begin{cases}
\dfrac{V\phi_{e,\text{OM}}}{RT}\dfrac{\partial p_1}{\partial t} + V\dfrac{\rho_{\text{OM}}V_{L,\text{OM}}\rho_{g1,stp}}{M_1}\dfrac{\partial \theta_1}{\partial t} = -\iiint\limits_V \nabla \vec{N}_1 dV \\[3mm]
\dfrac{V\phi_{e,\text{OM}}}{RT}\dfrac{\partial p_2}{\partial t} + V\dfrac{\rho_{\text{OM}}V_{L,\text{OM}}\rho_{g2,stp}}{M_2}\dfrac{\partial \theta_2}{\partial t} = -\iiint\limits_V \nabla \vec{N}_2 dV,
\end{cases}
\quad\quad (2)
$$

where $\phi_{e,\text{OM}}$ is the effective porosity of OM; ρ_{OM} is the density of OM ($1300\,\text{kg/m}^3$); $\rho_{g1,stp}$ and $\rho_{g2,stp}$ are the density of $^{13}\text{CH}_4$ and $^{12}\text{CH}_4$ in the standard condition, respectively; and $V_{L,\text{OM}}$ is the ultimate adsorbed amount in terms of OM. θ_i is the surface coverage of gas component i, which will be explained in detail later in the text. The time partial derivative of the adsorption term can be replaced by the form of pressure, which gives

$$
\frac{\partial \theta_i}{\partial t} = \frac{\partial \theta_i}{\partial p_1}\frac{\partial p_1}{\partial t} + \frac{\partial \theta_i}{\partial p_2}\frac{\partial p_2}{\partial t}. \quad\quad\quad\quad\quad\quad\quad\quad\quad\quad\quad\quad\quad\quad\quad\quad\quad\quad (3)
$$

Finally, we obtain the equation with the partial pressures as its unknowns,

$$
\begin{bmatrix} \dfrac{\partial p_1}{\partial t} \\[3mm] \dfrac{\partial p_2}{\partial t} \end{bmatrix} = A^{-1}\begin{bmatrix} -\iiint\limits_V \nabla \vec{N}_1 dV \\[3mm] -\iiint\limits_V \nabla \vec{N}_2 dV \end{bmatrix}, \quad\quad\quad\quad\quad\quad\quad\quad\quad\quad\quad\quad\quad\quad\quad (4)
$$

where A can be expressed as

$$
A = \begin{bmatrix} V\dfrac{\rho_{\text{shale}}V_L\rho_{g1,stp}}{M_1}\dfrac{\partial \theta_1}{\partial p_1} + \dfrac{V\phi_{e,\text{OM}}}{RT}, & V\dfrac{\rho_{\text{shale}}V_L\rho_{g1,stp}}{M_1}\dfrac{\partial \theta_1}{\partial p_2} \\[3mm] V\dfrac{\rho_{\text{shale}}V_L\rho_{g2,stp}}{M_2}\dfrac{\partial \theta_2}{\partial p_1}, & V\dfrac{\rho_{\text{shale}}V_L\rho_{g2,stp}}{M_2}\dfrac{\partial \theta_2}{\partial p_2} + \dfrac{V\phi_{e,\text{OM}}}{RT} \end{bmatrix}. \quad\quad (5)
$$

Eq. 4 is solved by the explicit-scheme finite-volume method to obtain the partial pressures of the isotopes during the entire degassing process.

Third, we calculate the gas content and recovery. First, the remaining gas at time t of the isotopes is calculated.

In IOM, only the free gas is considered, and the remaining gas amount is

$$G_i(t) = \sum_k \left[\frac{V_k p_{ik}(t) \phi_{e,IOM}}{RT} \right]. \quad \dots\dots\dots\dots\dots\dots\dots\dots\dots\dots\dots\dots\dots\dots\dots\dots\dots\dots\dots\dots \quad (6)$$

In OM, both the free gas and adsorption gas are involved, which gives

$$G_{i,OM}(t) = \sum_k \left[\frac{V_k p_{ik}(t) \phi_{e,OM}}{RT} + \frac{V_k \rho_{OM} V_{L,OM} \rho_{gi,stp}}{M_i} \theta_{ik}(t) \right]. \quad \dots\dots\dots\dots\dots\dots\dots\dots\dots\dots\dots\dots\dots \quad (7)$$

Thus, the gas content can be expressed as $G = \sum\limits_{i=1,2} G_{i,IOM}(t=0) + G_{i,OM}(t=0)$. Finally, the gas recovery of methane at time t is

calculated by $E(t) = \dfrac{G - \left[\sum\limits_{i=1,2} G_{i,IOM}(t) + G_{i,OM}(t) \right]}{G}$.

Isotopic Composition. The isotopic composition of methane is calculated from the pressure ratio or molar ratio of $^{13}CH_4$ and $^{12}CH_4$, using

$$\delta = \left[\frac{(^{13}C/^{12}C)_{gas}}{(^{13}C/^{12}C)_{standard} - 1} \right] \times 1{,}000. \quad \dots\dots\dots\dots\dots\dots\dots\dots\dots\dots\dots\dots\dots\dots\dots\dots\dots\dots\dots \quad (8)$$

The widely used standard is Peedee Belemnite (PDB; Urey 1947), with $(^{13}C/^{12}C)_{standard} = 0.011237$.

Because the isotopic composition of expelled gas changes with time, there is both a differential value (instantaneous, δ_{ins}) and an integral average value (cumulative, δ_{cum}) for expelled gas. The former refers to the gas expelled at each time point; the latter refers to the gas cumulatively trapped from the beginning of the degassing until a certain time point.

The value of δ_{ins} at time t is calculated from the degassing rate of the isotopes as

$$\delta_{ins}(t) = \left[\frac{q_1(t)/q_2(t)}{(^{13}C/^{12}C)_{standard}} - 1 \right] \times 1{,}000, \quad \dots\dots\dots\dots\dots\dots\dots\dots\dots\dots\dots\dots\dots\dots\dots\dots \quad (9)$$

where $q_1(t)$ and $q_2(t)$ are the degassing rate of $^{13}CH_4$ and $^{12}CH_4$ at time t (in mol/s).

The value of δ_{cum} at time t is calculated from the amount of expelled isotopes as

$$\delta_{cum}(t) = \left[\frac{Q_1(t)/Q_2(t)}{(^{13}C/^{12}C)_{standard}} - 1 \right] \times 1{,}000, \quad \dots\dots\dots\dots\dots\dots\dots\dots\dots\dots\dots\dots\dots\dots\dots\dots \quad (10)$$

where $Q_1(t)$ and $Q_2(t)$ are the cumulative degassing amount of $^{13}CH_4$ and $^{12}CH_4$, respectively, at time t (in mol).

Gas-Transport Mechanism and Fractionation

Transport Mechanism. In BG-CDAM, gas flow in the shale is modeled with the consideration of viscous flow, Knudsen diffusion, and competitive adsorption (**Fig. 2**).
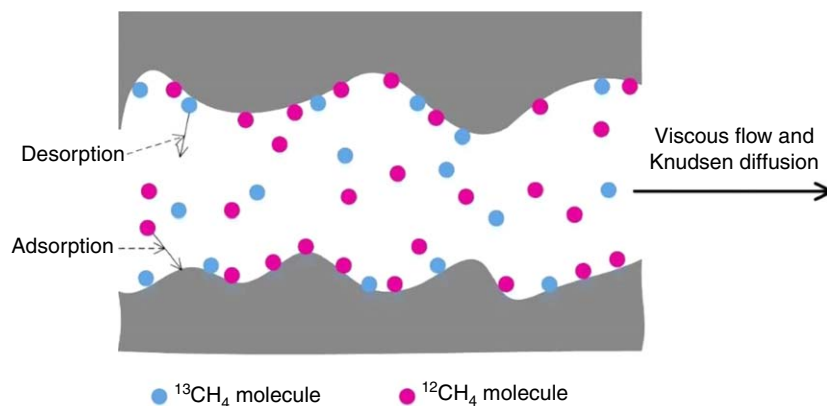

Fig. 2—Schematic of transport mechanism.

Shale has low porosity and low permeability, with the development of nanopores. The continuity assumption for Darcy flow becomes invalid and the gas-flow regime depends on the Knudsen number (Kn). The Knudsen number is defined as the ratio of the molecular mean free path of a gas molecule to the average height or the diameter of the pore. The gas-flow regimes in nanopores are continuous flow ($Kn < 10^{-3}$), slip flow ($10^{-3} < Kn < 10^{-1}$), transition flow ($10^{-1} < Kn < 10$), and Knudsen diffusion ($Kn > 10$). Viscous flow is caused by intermolecular collision, whereas Knudsen diffusion is caused by collision between the molecules and nanopore walls, and slip flow is a regime in which both types of collisions exist simultaneously and either of them can be ignored. Because the Knudsen number changes with the pore diameter and gas pressure, it is reasonable to consider such changes in the degassing process. In recent years, a large number of researchers have noticed the non-Darcy effect in shale. Civan (2002) and Civan et al. (2010) proposed

apparent-permeability models as a function of the Knudsen number, incorporating several empirical parameters. Javadpour (2009) developed a model using the superposition of viscous flow, slip flow, and Knudsen diffusion, which is relatively complete and widely used with some extensions (Darabi et al. 2012; Naraghi et al. 2015). Rahmanian et al. (2012) proposed an empirical formula by summing viscous flow and Knudsen diffusion using weight coefficients. Moreover, other researchers added the surface diffusion of adsorption gas into shale-gas transport (Song et al. 2016). However, those phenomenological models are superposition forms of different mechanisms. The rationality of some models is under debate because of their insufficiency to address the coupled effect (Wu and Zhang 2016). In addition, these studies all deal with single-component gas (mostly pure methane) without involving the non-Darcy flow of multicomponent gas. The empirical parameters or weight coefficients in those models are difficult to determine for $^{13}CH_4$ and $^{12}CH_4$. The formulas are also questionable in the simulation for the fractionation process of carbon isotopes of methane. Other researchers use molecular-dynamics simulations to investigate nanoscale mechanisms when considering transport coupled with adsorption (Wu and Zhang 2016), which also has limitations in calculation scales and computing expense. The most widely used model for the flow of mixed gas is the dusty-gas model (DGM) (Krishna 1993; Allan et al. 2004; Weber and Newman 2005; Ding et al. 2017). The DGM can integrate the effects of viscous flow and Knudsen diffusion considering the partial pressures of carbon isotopes of methane. It is believed that the slip flow is a regime where both viscous flow and Knudsen diffusion coexist simultaneously, so it is not independent from DGM. We believe the main influence of adsorption for fractionation is caused by the differences in adsorption/desorption of $^{13}CH_4$ and $^{12}CH_4$, and the mobility differences of the adsorbed isotopes have a smaller effect. Moreover, one of the main objectives of this study is comparing the effects of diffusion and adsorption/desorption on fractionation. Because this is the first time calculating the fractionation when considering different specific microscale mechanisms, we are cautious in the selection of simulation models in case of export-error recognition and will also compare the simulated and measured results to analyze accuracy. With this understanding, we adopt DGM in this study to calculate the flow flux as

$$N_i = -\frac{\nabla p_i}{RT}\frac{\phi_f}{\tau}\left(D_{K,i} + \frac{pr^2}{8\mu}\right), \quad \ldots \ldots \ldots \ldots \ldots \ldots \ldots \ldots \ldots \ldots \ldots \ldots \ldots \ldots \ldots \ldots \ldots (11)$$

where τ is tortuosity, r is pore radius, μ is gas viscosity, p is the total pressure of the mixed gas $\left(p = \sum_i p_i, \nabla p_i = p\nabla x_i + x_i\nabla p\right)$, and x_i is the mole fraction of the gas component i. ϕ_f is the flow porosity; gas flow is controlled by the narrow pores in the heterogeneous porous media, and the flow porosity is the volume fraction of those narrow pores. The definitions of total porosity, effective porosity, and flow porosity are shown in **Fig. 3.** Many nanopores and throats, which form pore networks, develop in OM, and the gas flow is controlled by its flowing porosity $\phi_{f,OM}$ in Eq. 11, whereas the gas storage is controlled by its effective porosity $\phi_{e,OM}$ in Eq. 2. We consider IOM as a flow path with negligible storing space and suppose an equal effective porosity and flow porosity for it ($\phi_{f,IOM} = \phi_{e,IOM}$). $D_{K,i}$ is the Knudsen diffusivity, calculated as

$$D_{K,i} = \frac{2r}{3}\sqrt{\frac{8RT}{\pi M_i}}, \quad \ldots \ldots \ldots \ldots \ldots \ldots \ldots \ldots \ldots \ldots \ldots \ldots \ldots \ldots \ldots \ldots \ldots \ldots \ldots \ldots \ldots (12)$$

where M_i is the molecular weight of gas component i. Because the "unipore" model will induce errors, a pore-size distribution is used in this study, as given in Appendix A.
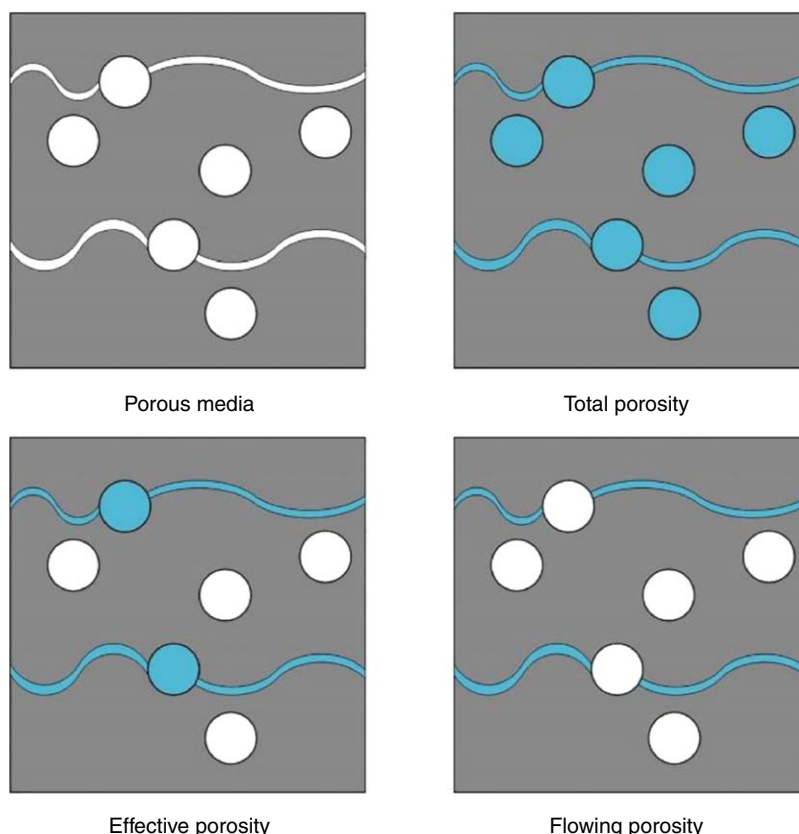

Fig. 3—Different porosity types of porous media.

Regarding adsorption, because of the different adsorption capacities of the isotopes, they will compete for the adsorption locations of the pore walls. The adsorption amounts of the isotopes are different at the same pressure. In this study, the extended Langmuir adsorption model is adopted to involve the competitive adsorption. The model is computationally simple, without iterative solution. Although the model supposes a monolayer adsorption that will bring errors, molecular-dynamics simulations show that the adsorption layer closest to the wall is dominant, especially at pressures less than 30 MPa (Jiang and Lin 2017). Using the extended Langmuir adsorption model, the surface coverage of gas component i can be calculated by

$$\theta_i = \frac{b_i p_i}{1 + \sum_{j=1}^{n} b_j p_j}, \quad \dots\dots\dots\dots\dots\dots\dots\dots\dots\dots\dots\dots\dots\dots\dots \quad (13)$$

where $b_i = K_i/p^0$, in which p^0 is standard pressure at 1 bar and K_i is the Langmuir coefficient of gas component i. For $^{12}CH_4$, $K_2 = K_a/K_d = \exp\left(\frac{q}{RT} + \frac{\Delta s^0}{R}\right)$, where q is the heat of adsorption and Δs^0 is the standard entropy of adsorption. The values of $q = 15.1$ kJ/mol and $\Delta s^0 = 76.0$ J/mol/K are derived from isotherms reported in Xia and Tang (2012). For $^{13}CH_4$, $K_1 = \alpha K_2$, $\alpha = \exp\left(\frac{A}{T^2} - \frac{B}{T}\right)$, $A = 95.17K$, and $B = 0.125K$.

In this study, adsorption is assigned only in OM. The ultimate adsorption capacity of shale, $V_{L,shale}$, is obtained by high-pressure methane-isotherm-adsorption measurements and then converted into the terms of OM as

$$V_{L,OM} = \frac{V_{L,shale}\rho_{shale}}{\omega\rho_{OM}}, \quad \dots\dots\dots\dots\dots\dots\dots\dots\dots\dots\dots\dots\dots\dots\dots \quad (14)$$

where ρ_{shale} is shale density (2600 kg/m^3) and ω is volumetric TOC. The adsorption amount (in m^3/kg) of the gas component i in OM under the standard conditions is $V_{i,stp} = V_{L,OM}\theta_i$. Therefore, the amount of substance of the gas component i in the adsorbed phase per unit volume of OM is

$$n_{i,a} = \frac{\rho_{OM} V_{L,OM} \rho_{gi,stp}}{M_i} \theta_i. \quad \dots\dots\dots\dots\dots\dots\dots\dots\dots\dots\dots\dots\dots\dots\dots \quad (15)$$

Influence of Flow Mechanisms on Fractionation. In this subsection, we study the mechanisms of fractionation using a simplified form of BG-CDAM with "unipore" symmetric homogeneous spheres standing for the shale samples. The distinction between OM and IOM is ignored, and the pore radius is assumed to be uniform. The instantaneous isotope composition and the gas recovery during the degassing process are calculated, with the values of the basic parameters shown in **Table 1.**

Parameters	Values
Absolute temperature, T (K)	300
Gas Component 1	$^{13}CH_4$, 17g/mol
Gas Component 2	$^{12}CH_4$, 16g/mol
Initial pressure, p_{in} (MPa)	45
Tortuosity, τ	10
δ_0	−30
Boundary pressure (MPa)	0
Pore radius, r (nm)	2, 5, 10, 100
$V_{L,shale}$ (cm^3/g)	0.001
Shale-sample radius, L (mm)	1

Table 1—Values of the basic parameters in the mechanism analysis.

First, the fractionation with the pure Knudsen diffusion is calculated, as shown in **Fig. 4.** Then, the viscous flow and adsorption are added to the simulation. We find that the pore radius has a great influence on the fractionation process. Therefore, fractionations in the pores with $r = 2$ and 100 nm are calculated as shown in **Figs. 5 and 6,** respectively.

Fig. 4 shows that Knudsen diffusion causes an obvious fractionation. In the pure-diffusion process, the fractionation reflects the relative velocity ratio of the two gas components, and the δ_{ins}/E curves are nearly the same for different pore radii. Knudsen diffusion is dependent on the molecular weight of the gas, and the velocity ratio of $^{13}CH_4$ and $^{12}CH_4$ is $D_{K,1}/D_{K,2} = \sqrt{M_2/M_1} = 97\%$. $^{12}CH_4$ flows faster, which makes more $^{12}CH_4$ in the early period and more $^{13}CH_4$ in the later period, resulting in δ_{ins} increasing with time. For pure diffusion, the degassing gas monotonically becomes heavier over time. The analysis of the pure-diffusion process is consistent with the conclusion in the study of Xia and Tang (2012).

Figs. 5 and 6 shows the fractionations in the pores with $r = 2$ and 100 nm. The results provide a clear comparison of the contributions of diffusion, convection, and adsorption/desorption. The results illustrate the following:

1. Diffusion: Knudsen diffusion is the main mechanism of fractionation, which causes the background increasing trend for δ_{ins}.
2. Convection: Viscous flow does not induce fractionation itself, but it brings significant gas flow under high pressures and a large pore radius, which reduces the variation range of the isotopic composition. In other words, viscous flow will weaken the fractionation, and this weakening effect becomes more pronounced with increasing pore-radius value.
3. Competitive adsorption: The competitive adsorption of the isotopes causes weak fractionation. The light isotope is preferentially desorbed, resulting in a decrease for δ_{ins}. For $r = 2$ nm, the curve becomes more negative. For $r = 100$ nm, there is a significant negative peak for δ_{ins}, which brings a lagging reversal. This behavior can be understood in this way: Because the variation of the

adsorption amount with pressure is small at a high-pressure condition, the adsorption effect is weak at the initial time; as the pressure decays, the fractionation caused by competitive adsorption becomes pronounced, and the δ_{ins}/E curve presents a negative peak. In the final stage, the Knudsen diffusion becomes dominant because of the low pressure.

4. The isotopic composition is sensitive to the pore radius, so treating shale with a single pore size will bring large errors, and it is necessary to consider the heterogeneous pore-size distribution in the fractionation for shale.

5. Comparing the results of the different pore sizes of Figs. 5 and 6, it is known that the fractionation is dominated by the small pores when considering the pore-size distribution. The pores with large radius will have relatively stronger viscous flow and have little effect on the fractionation process.
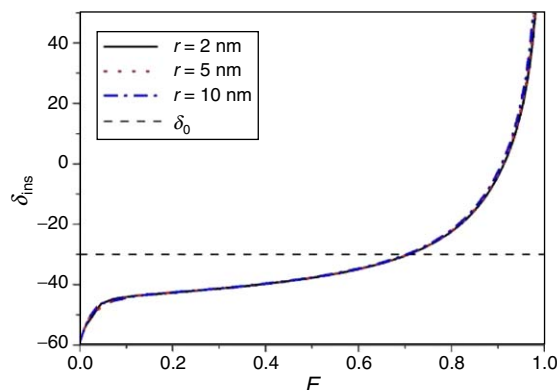
Fig. 4—Variation of δ_{ins} with gas recovery *E* considering only Knudsen diffusion.
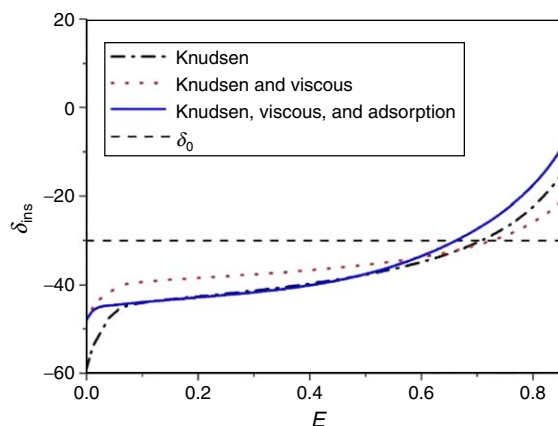
Fig. 5—Variation of δ_{ins} with gas recovery considering different flow mechanisms, with the pore radius of 2 nm.
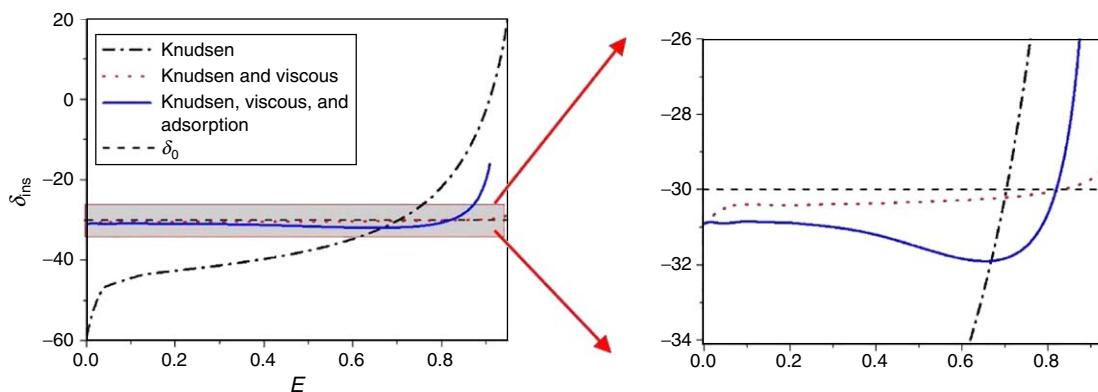
Fig. 6—Variation of δ_{ins} with gas recovery considering different flow mechanisms, with the pore radius of 100 nm.

Evaluating Gas Content and Identifying Sweet Spots

Sample and Isotope-Composition Measurement. We analyze shale samples taken from the Longmaxi Formation of the Lower Silurian and the Wufeng Formation of the Upper Ordovician in Well DY5 at the Dingshan District, Chongqing, China. The Longmaxi and Wufeng Formations are the major gas-producing shale formations in China. The basic parameters of the reservoir and sample are listed in **Table 2.** For the samples from different depths in Well DY5, the isotope-logging test is performed using the GC-IR[2] infrared

laser isotope spectrometer. GC-IR^2 is a new generation of isotope-measurement instrument independently developed by the Power Environmental Energy Research Institute. It is different from the commonly used isotope mass spectrometer (GC-MS) in the laboratory. Using GC-IR^2, the measurement of the C_{1-3} isotopes can be completed within 5 minutes and its accuracy is comparable with that of GC-MS. The absolute error of the measured relative abundance of $^{13}CH_4$ and $^{12}CH_4$ is less than 0.5‰, and the lower limit of the measured concentration is as low as 0.5 ppm. GC-IR^2 can be used in the gas field to achieve in-situ measurement of samples, making isotope logging possible.

Parameters	Values
Absolute temperature, T (K)	300
Initial pressure, p_{in} (MPa)	45
Volumetric TOC (vol%)	8.7%
δ_0	−28.40
Shale-sample radius, L (mm)	5
$V_{L,shale}$ (in terms of shale mass) (m^3/kg)	0.004
τ	10
Lost time (minutes)	15

Table 2—Basic parameters of the reservoir and sample.

The procedure of the isotope-logging test is shown in **Fig. 7.** At first, the shale samples from shale formations are brought to the ground through mud circulation, and the mud gas is collected immediately. Mud gas is actually the gas released from the formation in drilling and is mainly composed of gas from the broken rocks, which reflects the most-intuitive isotope information of the drilling formation. Because shale gas has poor fluidity and typical in-situ storage characteristics, the isotope fractionation caused by diffusion in the returning of the mud is not obvious. It is believed that mud gas can be directly considered as the gas in the in-situ formation. Therefore, we take the isotopic composition of mud gas as the true value of the isotopic composition of the sample, or δ_0. Second, the shale samples are sealed in the degassing canister. The headspace gases in the degassing canister are collected at a sequence time. The carbon-isotope compositions of the headspace gases in the degassing process are then measured using GC-IR^2. Because the headspace gas is cumulative, the measured isotopic composition is also a cumulative value as δ_{cum}, defined in Eq. 10. Finally, the figure of variation of δ_{cum} with time is obtained, as shown in Fig. 7.
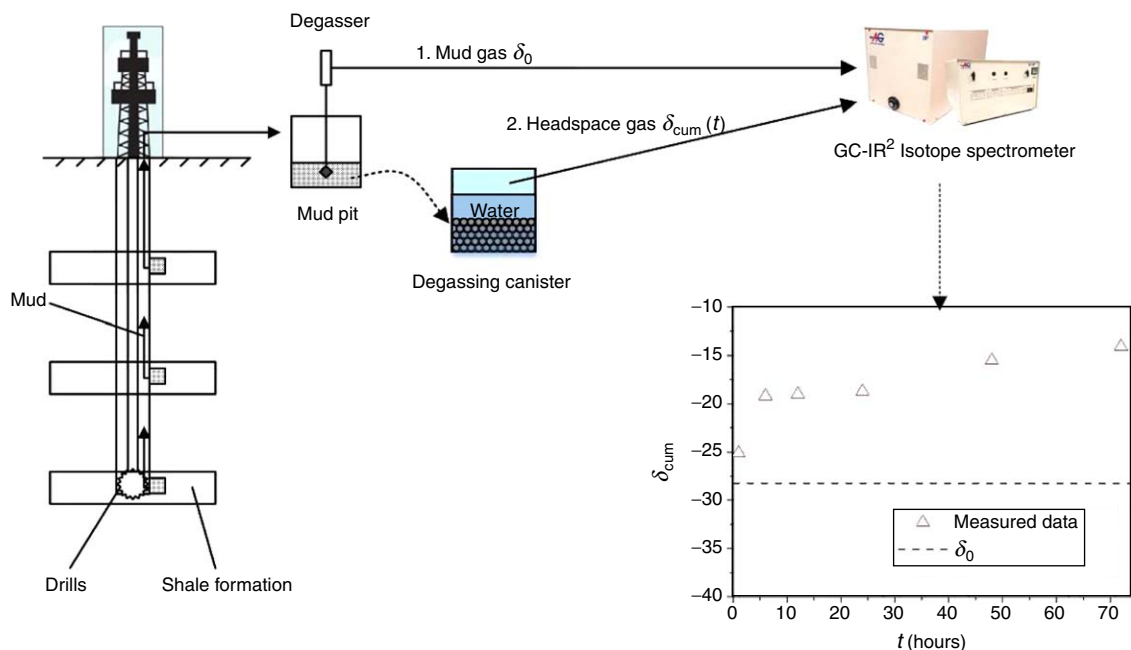

Fig. 7—Procedure of the isotope-logging test.

Matching the Simulated and Measured Data. The parameters in Eqs. 1 and 2 need to be calibrated before the model can be applied to the evaluation for shale-gas content. Most of the parameters, such as initial and boundary conditions, sample geometry, density, TOC, and ultimate adsorption amount, can be measured. The only unknown parameters in the model are the porosities of $\phi_{e,OM}$, $\phi_{f,OM}$, and $\phi_{e,IOM}$. Because the parameters of Eqs. 1 and 2 can largely be known, the model can be rigorously calibrated. Because $\phi_{e,OM}$, $\phi_{f,OM}$, and $\phi_{e,IOM}$ are not available, we used an optimization scheme to derive them by matching the calculated time-dependent isotopic composition with the measured data. The matching problem is given as

$$\begin{cases} \text{minimize} \sum (\delta_{cum,\text{BG-CDAM}} - \delta_{cum,\text{Measurement}})^2 \\ \text{subject to } \vec{\alpha}_{min} \leq \vec{\alpha} \leq \vec{\alpha}_{max}, \end{cases} \quad \dots \dots \dots \dots \dots \dots \dots \dots \dots \dots \dots \dots \dots \text{(16)}$$

where $\delta_{cum,BG\text{-}CDAM}$ and $\delta_{cum,Measurement}$ are the cumulative isotopic composition of the simulation and the measurement and $\vec{\alpha}$ is the unknown vector ($\phi_{e,OM}$, $\phi_{f,OM}$, and $\phi_{e,IOM}$). The subscripts "min" and "max" denote the lower and upper bounds, respectively. Considering the low porosity and low permeability of shale, we give the lower and upper bounds according to the focused-ion-beam–scanning-electron-microscope images for many shale samples from the Longmaxi Formation (Cao et al. 2017, 2018): $\vec{\alpha}_{min} = (0, 0, 0)$ and $\vec{\alpha}_{max} = (20\%, 5\%, 2\%)$.

At first, the effects of the unknown parameters on the fractionation are analyzed to guide the matches. Take the sample from the Long 1_1 submember of the Longmaxi Formation in Well DY5 as an example. The TOC content of the example sample is 4.36. The pore-size distribution of the sample is obtained by a nitrogen-adsorption test, as shown in **Fig. 8.** The pore-size distribution of the sample shows a tendency of multipeaks. According to the results obtained by scanning images of the sample, the peaks below 30 nm are classified as organic pores, whereas the peak above 30 nm appears to be normal distribution and is classified as inorganic pores. The fractionation process is dominated by these four peaks, and thus the volume fractions of these peaks are calculated from the pore-size distribution. The dominant pore sizes of the organic and inorganic pores and their respective proportions are obtained, as listed in **Table 3.** Calculating the fractionation process by the dominant pore size has a higher precision than using a single pore size or a determined diffusion coefficient. The ultimate adsorption amount of the sample is obtained by the high-pressure methane-isotherm-adsorption measurement. Using those inputs, the effects of the unknown parameters on the fractionation are calculated as follows.
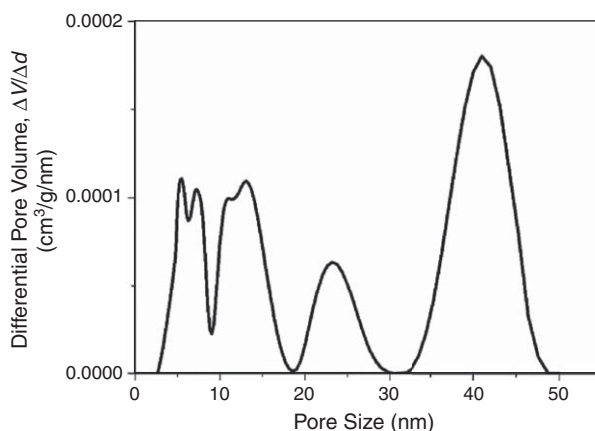

Fig. 8—Pore-size distribution of the example sample.

Pore Types	Peak Pore Size (nm)	Peak Pore Radius (nm)	Percentage in Organic/Inorganic Pores (%)
	6	3	0.3031
Organic pore	13	6.5	0.4233
	24	12	0.2736
Inorganic pore	41	20.5	1

Table 3—Dominant pores of the pore-size distribution of the example sample.

Effective Porosity of OM ($\phi_{e,OM}$). **Fig. 9** shows that the isotopic compositions change with time under different $\phi_{e,OM}$ values. The δ_0 curve is also added to Fig. 9 to better describe the behavior of the system. Fig. 9a demonstrates that an increase in $\phi_{e,OM}$ will increase δ_{cum}. The results suggest that high cumulative isotopic composition will accompany high porosity for gas storage in OM. δ_{cum} has a relatively fast increase at first and then tends to be stable; this is because the releasing gas amount becomes less and less as the pressure drops, and finally it will reach a steady state with a constant isotopic composition. Fig. 9b presents the variation of δ_{ins} with E. After a negative peak caused by adsorption, δ_{ins} has an approximately exponential growth as Knudsen diffusion becomes dominant because of the dropping pressure. To better clarify, we define the gas recovery at the turning point in the δ_{ins}/E curve, E_t, where δ_{ins} changes from lower to higher than δ_0. Fig. 9b shows that with the increase of $\phi_{e,OM}$, E_t increases. In addition, because of the difference of OM and IOM in shale, the fractionation shows a two-stage process. In the first stage, the isotope composition has a weak variation resulting from the relatively large pores in IOM; in the second stage, the gas fractionation becomes pronounced and a negative peak of δ_{ins} appears with the Knudsen diffusion and competitive adsorption in OM. Fig. 9b also shows that $\phi_{e,OM}$ mainly affects the second stage of degassing, whereas the first stage is controlled by IOM. When $\phi_{e,OM}$ increases, the free-gas volume increases, and so the ratio of free gas to adsorbed gas will also increase. When the ultimate adsorption amount is fixed, a smaller $\phi_{e,OM}$ will lead to a larger percentage of adsorbed gas, resulting in a weaker fractionation caused by competitive adsorption. Because the adsorption-inducing fractionation reduces the isotopic composition, as shown in Figs. 5 and 6, the negative peak of δ_{ins}/E is lower in a smaller $\phi_{e,OM}$. In addition, Fig. 9b shows that the δ_{ins}/E curves of different $\phi_{e,OM}$ values coincide at a recovery of 66%.

Flowing Porosity of OM ($\phi_{f,OM}$). **Fig. 10** shows that as the $\phi_{f,OM}$ increases, the δ_{cum} becomes more positive and E_t becomes larger. It can be also seen from Fig. 10b that $\phi_{f,OM}$ affects the second stage of the degassing process, which is the degassing in OM. $\phi_{f,OM}$ has a great influence on the mass transport in OM, but it has no direct correlation with gas content. Changing $\phi_{f,OM}$ will cause a complicated effect on the pressure-decay process and the percentages of free-gas and adsorbed-gas changes in time, which bring a variation in the degassing rate of $^{13}CH_4$ and $^{12}CH_4$.

Effective Porosity of IOM ($\phi_{e,IOM}$). **Fig. 11** shows that increasing $\phi_{e,IOM}$ will increase δ_{cum}, but their E_t values are close. It can be also seen from Fig. 11b that the variation of $\phi_{e,IOM}$ causes a large difference in isotope compositions because it affects the degassing at the early stage in IOM. The greater the $\phi_{e,IOM}$, the larger the range of recovery occupied by the first stage because increasing inorganic porosity will increase the gas amount in IOM.
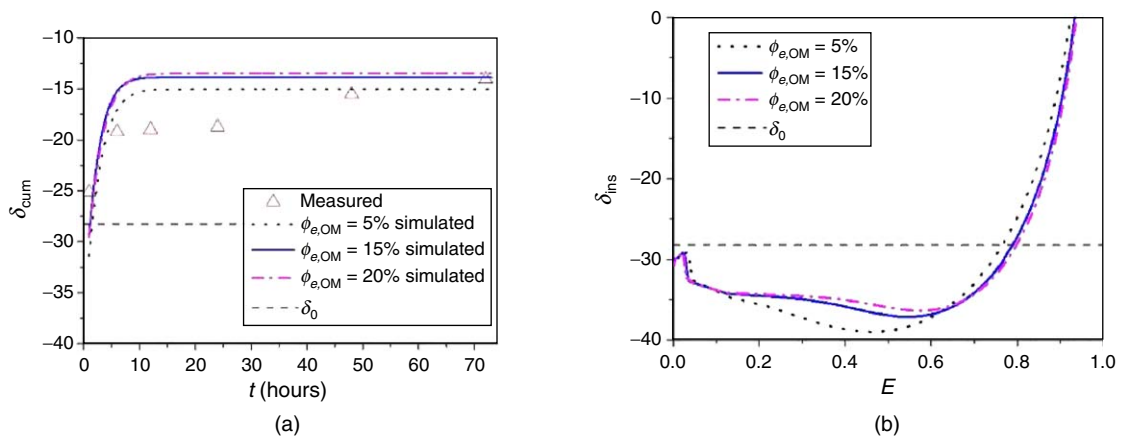
Fig. 9—Effect of $\phi_{e,\text{OM}}$ on fractionation: (a) variation of δ_{cum} with time t; (b) variation of δ_{ins} with E.
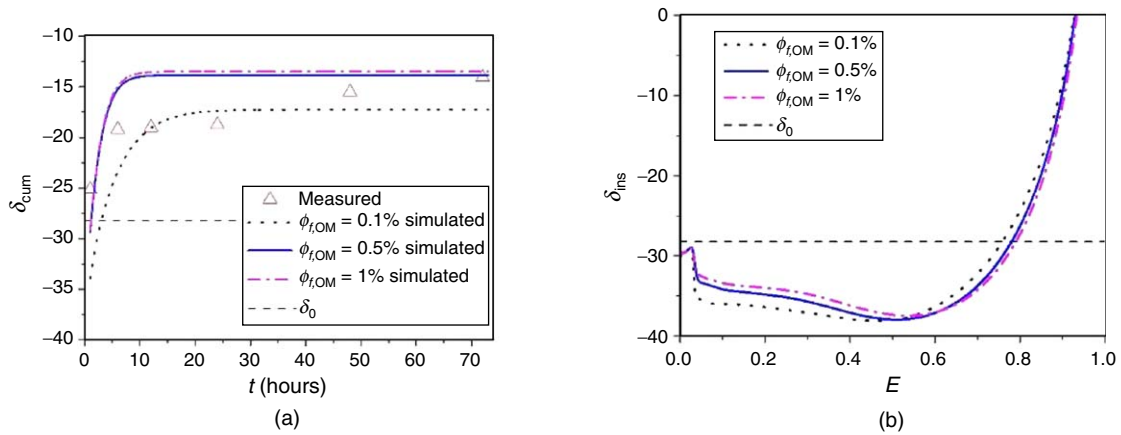

Fig. 10—Effect of $\phi_{f,\text{OM}}$ on fractionation: (a) variation of δ_{cum} with time t; (b) variation of δ_{ins} with E.
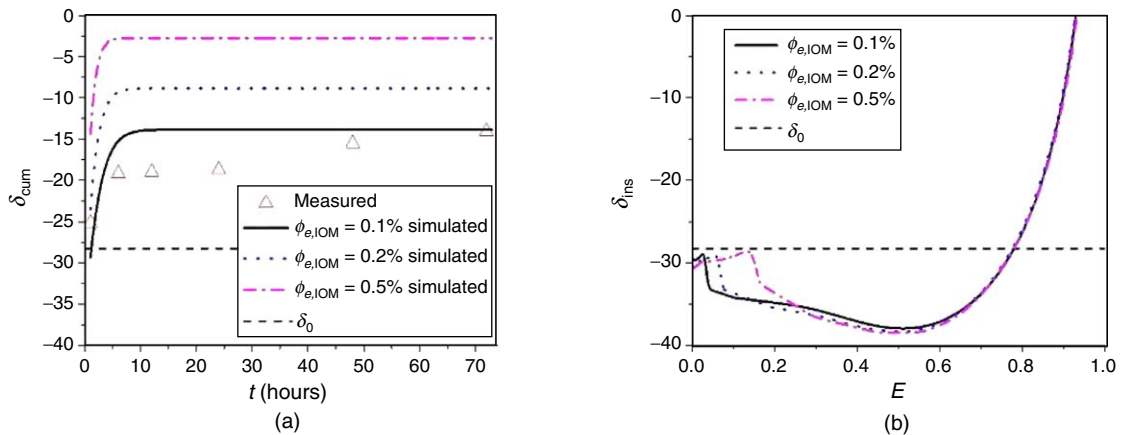

Fig. 11—Effect of $\phi_{e,\text{IOM}}$ on fractionation: (a) variation of δ_{cum} with time t; (b) variation of δ_{ins} with E.

After those analyses, the matching is optimized by a gradual adjustment of the values of the porosities. Because the calculated results are from a finite-volume-method simulator, it is difficult to accurately update the porosities using a computer in the matching. Therefore, we set a series of porosity values to simultaneously simulate using parallel computing and then chose the best matching results. The final matching result is shown in **Fig. 12,** with $\vec{\alpha} = (15\%, 0.5\%, 0.1\%)$. Results show that the simulated values are in good agreement with the measured data in isotope logging for the example sample.

Evaluation of Gas Content. After all the unknown parameters are obtained, the gas content of the example sample is calculated using the basic parameters in Table 3 and $\vec{\alpha} = (15\%, 0.5\%, 0.1\%)$ fitted in Fig. 12. The gas content of the sample is $3.70\,\text{m}^3/\text{t}$, wherein the free gas is $1.37\,\text{m}^3/\text{t}$ and the adsorbed gas is $2.33\,\text{m}^3/\text{t}$. In addition, the variation of gas recovery with time is also shown in **Fig. 13.**

Results show that the percentages of lost, degassing, and residual gas are 69, 30, and 1%, respectively. Results also suggest that isotope fractionation does provide a new way to evaluate shale-gas content. More importantly, it has the characteristics of the existing direct method and the indirect method for gas-content evaluation: On the one hand, the amounts of lost, degassing, and residual gas can be obtained, but on the other hand, the free and adsorbed gases can also be determined.
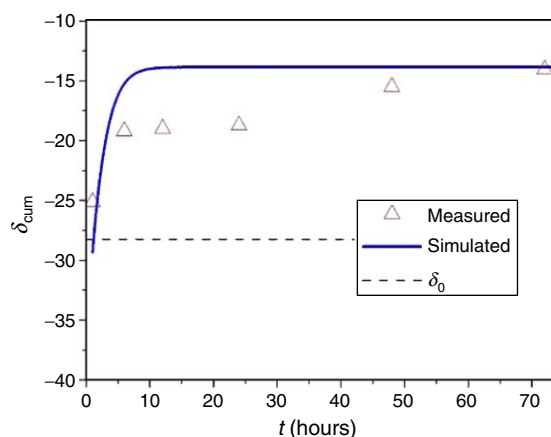

Fig. 12—Matching results of the simulated and measured data.
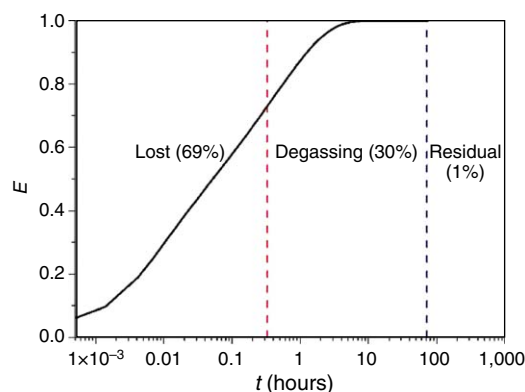
Fig. 13—Variation of gas recovery with time.

In addition, we plot the instantaneous isotopic composition as a function of recovery, as shown in **Fig. 14.** Results show that the turning point E_t is at approximately 80% gas recovery, E. The results also suggest that the corresponding relationship between δ_{ins} and E can be obtained according to the parameters obtained by matching the isotope-logging measurement. According to such a correspondence relationship, the remaining resources of a shale-gas well can be estimated by the recovery using the δ_{ins}/E curve through the measured δ_{ins} in its production process. This method is completely feasible in theory, and once implemented, it will have the characteristics of economical and rapid evaluation of the remaining resources in the producing well.
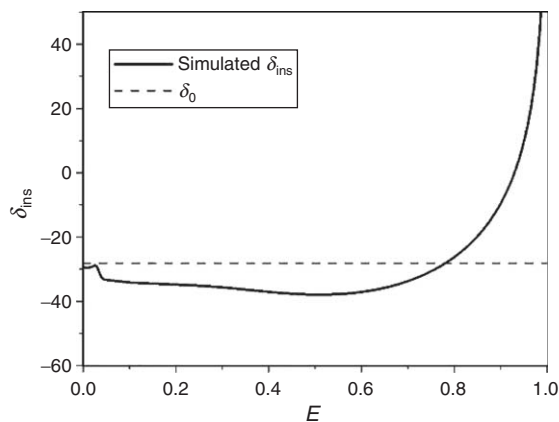

Fig. 14—Variation of δ_{ins} with gas recovery E.

Identification of Sweet Spots. In this subsection, to identify the sweet spots, four samples from different formations in Well DY5 are evaluated, and their basic parameters are shown in **Table 4.** In Well DY5, the high-quality shale formations mainly consist of the lower part of the Longmaxi Formation (Long 1 member) and the Wufeng Formation. The Long 1 member is subdivided into three submembers (Long 1_1, Long 1_2, Long 1_3), as shown in **Fig. 15a.** These samples are subjected to nitrogen-adsorption tests to obtain their pore-size distributions, as shown in Fig. 15b. It can be seen that the pore-size distributions of different shale samples have multipeak phenomena less than 30 nm, but the peak greater than 30 nm is single and demonstrates an approximately normal distribution. In this paper, the organic pores and inorganic pores are distinguished by 30 nm, and then the dominant pore size is extracted using the method in Table 3.

Shale Formation	Long 1_3 Submember	Long 1_2 Submember	Long 1_1 Submember	Wufeng Formation
TOC (wt%)	0.51	1.15	4.36	4.36
Volumetric TOC (vol%)	1.0%	2.3%	8.7%	8.7%
δ_0	−29.66	−29.98	−28.40	−29.61
$V_{L,shale}$ (cm³/g)	1.84	2.32	4.00	3.21
Specific surface area (m²/g)	17.4	15.1	28.8	19.5

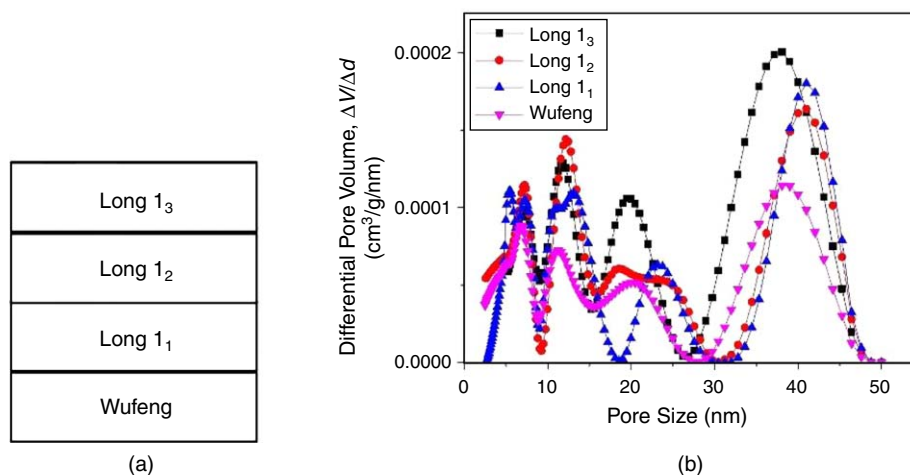Table 4—Basic parameters of the four samples from different formations.

Fig. 15—(a) Schematic of the shale formations; (b) pore-size distribution of samples from different formations.

The isotopic compositions of the samples from different formations are measured, and then their gas contents are separately calculated. The measured and simulated results are both shown in **Fig. 16,** and the matching parameters and the gas contents are listed in **Table 5.** The model proposed in this paper demonstrates good agreement overall with the test results. The simulation runs fast, with only 2 to 5 minutes for one case. Fig. 16 shows an apparent "high discrepancy" between the measured data and the prediction results at times shorter than 20 hours. In fact, the isotope composition is a conversion parameter from the relative abundance of isotopes, as shown in Eq. 8. The abundance of $^{13}CH_4$ is an extremely small value of approximately 1%. The unknown parameters in the simulation are the partial pressure and the isotope composition. Therefore, it is more reasonable to compare the original parameters of the measured data and the simulation in the deviation analysis. The relative deviation between the relative abundances of the measured and simulated data is calculated as

$$d = \frac{\left|(^{13}C/^{12}C)_{simulated} - (^{13}C/^{12}C)_{measured}\right|}{\left(^{13}C/^{12}C\right)_{measured}}. \qquad\qquad (17)$$
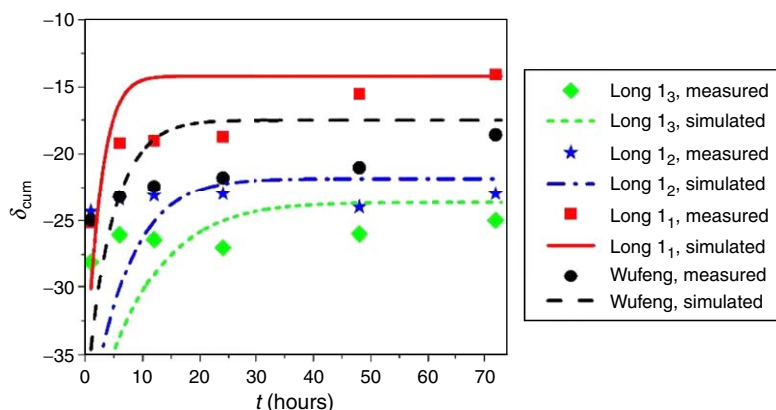

Fig. 16—Measured and simulated δ_{cum} of the samples from different formations.

Formation	Long 1_3 Submember	Long 1_2 Submember	Long 1_1 Submember	Wufeng Formation
$\phi_{e,OM}$	5%	10%	15%	10%
$\phi_{f,OM}$	0.05%	0.1%	0.5%	0.1%
$\phi_{f,IOM}$	0.05%	0.05%	0.1%	0.1%
Gas content (m^3/t)	1.28	1.69	3.70	2.82
Gas Composition 1 — Adsorption gas (m^3/t)	1.02	1.34	2.33	1.86
Gas Composition 1 — Free gas (m^3/t)	0.26	0.35	1.37	0.96
Gas Composition 2 — Lost gas	40%	51%	69%	61%
Gas Composition 2 — Degassing gas	59%	48%	30%	38%
Gas Composition 2 — Residual gas	1%	1%	1%	1%

Table 5—Gas contents of the samples from different formations.

The deviation results of the four samples are calculated as shown in **Fig. 17,** which shows that the relative deviations between the measured and simulated data are within 1.6%. The relative deviations after 20 hours are smaller, with the values being within 0.5%, which shows that the proposed method for organic-rich shale is valid and useful. The method does provide a completely new complement to the existing gas-content-analysis methods.
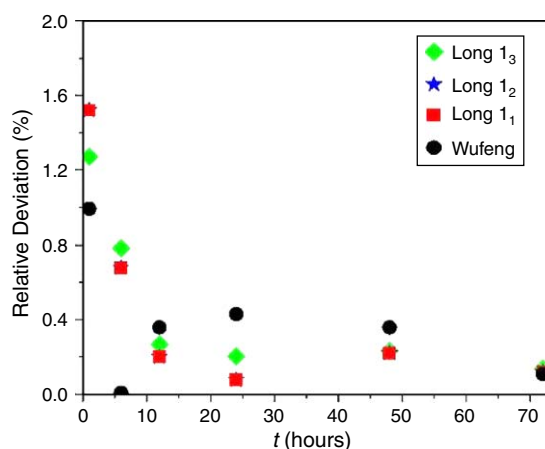

Fig. 17—Relative deviation between the relative abundances of the measured and simulated data.

The comprehensive results of Fig. 16 and Table 5 demonstrate the following:
1. The amount of adsorbed gas accounts for a large proportion of the gas content, accounting for approximately 60 to 80%.
2. On the other hand, the amount of lost gas also accounts for a large proportion of the gas content, from 40 to 70%.
3. The isotope values have a trend: Long 1_1 submember > Wufeng Formation > Long 1_2 submember > Long 1_3 submember. A relatively high cumulative isotopic composition is accompanied with high effective porosity. Results also show that the rank of gas content is the same as the isotope values: Long 1_1 submember > Wufeng Formation > Long 1_2 submember > Long 1_3 submember. Therefore, the Long 1_1 submember and Wufeng Formation are the potential sweet spots.

Integrating the results of isotopic composition and gas content, it is suggested that the formation with a more-positive isotopic composition in the isotope logging shows a higher gas content, which can provide a qualitative method for the identification of sweet spots in the field. Using the method proposed in this study, the quantitative gas content can be determined.

Conclusions
In this study, a new method for the evaluation of gas content using the carbon-isotope fractionation of methane is proposed. The flow chart of the method is shown in **Fig. 18.** First, the DGM and competitive adsorption are combined to establish the transport system in nanopores for shale. Then, a BG-CDAM is successfully established with a heterogeneous pore-size distribution and distinction of OM and IOM. Finally, depending on the isotope-logging measured values, the unknown parameters for gas-content calculation in BG-CDAM are obtained. By comparing the gas contents of samples from different formations, the sweet spots of an actual well are identified.

The findings show that the proposed method for organic-rich shale is valid and useful. The method carefully considers the microscopic flow mechanism of the isotopes of methane, which provides a solid foundation. A detailed understanding of the mechanism of fractionation of the isotopes is obtained for the first time, and the Knudsen-diffusivity difference is identified as the dominant factor. The logging-test data are introduced, which give a practical application background and real physical conditions. Through the proposed method in this study, not only can the lost, degassing, and residual gases be obtained, but also the free and adsorption gases can be calculated. The proposed method combined the basic mechanics theory and the logging-test practice of a carbon isotope, which shows a great application potential. In conclusion, the method provides a completely new complement to the existing gas-content-analysis methods. Moreover, the method might also have the potential to economically and rapidly evaluate the remaining resources in producing wells in future applications.
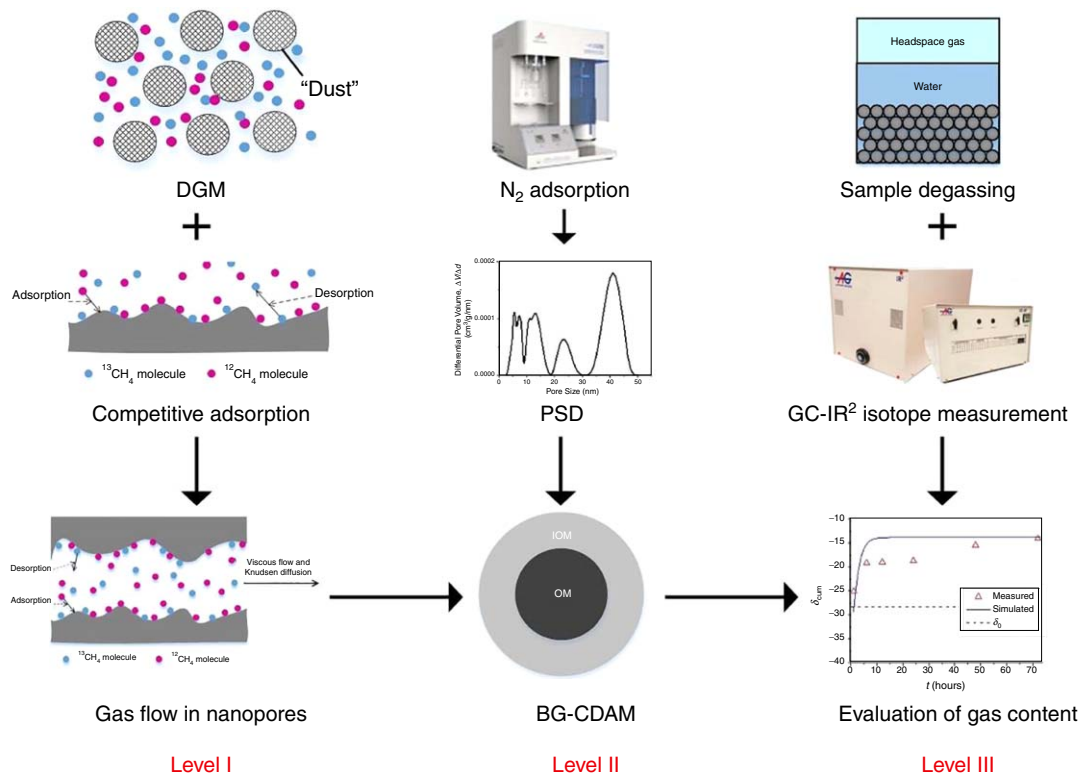
Fig. 18—Flow chart of the method in this study. PSD = pore-size distribution.

Nomenclature

d = relative deviation between the measured and simulated data, dimensionless
$D_{K,i}$ = Knudsen diffusivity of gas component i, m^2/s
E = gas recovery, dimensionless
E_t = gas recovery at the turning point in the δ_{ins}/E curve, dimensionless
G = gas content, mol
$G_{i,IOM}$ = remaining gas amount of gas component i in IOM, mol
$G_{i,OM}$ = remaining gas amount of gas component i in OM, mol
K_i = Langmuir coefficient of gas component i, dimensionless
M_i = molecular weight of gas component i, kg/mol
N_i = mass flux of gas component i, mol/(m^2·s)
p = total pressure of the mixed gas, Pa
p^0 = standard pressure, Pa
p_i = partial pressure of gas component i (i = 1 for ^{13}CH$_4$, i = 2 for ^{12}CH$_4$), Pa
p_{ik} = partial pressure of gas component in grid k, Pa
q = heat of adsorption, J/mol
q_i = degassing rate of gas component i, mol/s
Q_i = cumulative degassing amount of gas component i, mol
r = pore radius, m
R = universal gas constant, J/mol·K
R = time, seconds
T = absolute temperature, K
V = control volume, m^3
V_k = control volume of grid k, m^3
$V_{L,OM}$ = ultimate adsorbed amount in terms of OM, m^3/kg
$V_{L,shale}$ = ultimate adsorbed amount in terms of shale, m^3/kg
x_i = mole fraction of gas component i, dimensionless
α_j = volumetric faction for the pore r_j, dimensionless
δ = isotopic composition of methane, dimensionless
δ_{cum} = cumulative isotopic composition of methane, dimensionless
$\delta_{cum,BG-CDAM}$ = cumulative isotopic composition of the simulation using BG-CDAM, dimensionless
$\delta_{cum,Measurement}$ = cumulative isotopic composition of the isotope-well-logging measurement, dimensionless
δ_{ins} = instantaneous isotopic composition of methane, dimensionless
δ_0 = isotopic composition of methane in mud gas, dimensionless
Δs^0 = standard entropy of adsorption, J/mol/K
θ_{ik} = fractional adsorption coverage of gas component in grid k, dimensionless
μ = gas viscosity, Pa·s
$\rho_{gi,stp}$ = density of gas component i in the standard condition, kg/m^3
ρ_{OM} = density of OM, kg/m^3

ρ_{shale} = density of shale, kg/m^3
τ = tortuosity, dimensionless
$\phi_{e,IOM}$ = effective porosity of IOM, dimensionless
$\phi_{e,OM}$ = effective porosity of OM, dimensionless
ϕ_f = flow porosity, dimensionless
$\phi_{f,IOM}$ = flow porosity of IOM, dimensionless
$\phi_{f,OM}$ = flow porosity of OM, dimensionless
ω = volumetric TOC, vol%, dimensionless

Acknowledgments

References

Allan, F. M., Qatanani, N., Barghouthi, I. et al. 2004. Dusty Gas Model of Flow Through Naturally Occurring Porous Media. *Appl Math Comput* **148** (3): 809–821. https://doi.org/10.1016/S0096-3003(02)00939-6.

Cao, G., Lin, M., Jiang, W. et al. 2017. A 3D Coupled Model of Organic Matter and Inorganic Matrix for Calculating the Permeability of Shale. *Fuel* **204** (15 September): 129–143. https://doi.org/10.1016/j.fuel.2017.05.052.

Cao, G., Lin, M., Jiang, W. et al. 2018. A Statistical-Coupled Model for Organic-Rich Shale Gas Transport. *J Pet Sci Eng* **169** (October): 167–183. https://doi.org/10.1016/j.petrol.2018.05.033.

Civan, F. 2002. A Triple-Mechanism Fractal Model with Hydraulic Dispersion for Gas Permeation in Tight Reservoirs. Presented at the SPE International Petroleum Conference and Exhibition in Mexico, Villahermosa, Mexico, 10–12 February. SPE-74368-MS. https://doi.org/10.2118/74368-MS.

Civan, F., Rai, C. S., and Sondergeld, C. H. 2010. Shale-Gas Permeability and Diffusivity Inferred by Improved Formulation of Relevant Retention and Transport Mechanisms. *Transp Porous Med* **86** (3): 925–944. https://doi.org/10.1007/s11242-010-9665-x.

Cui, X., Bustin, A. M. M., and Bustin, R. M. 2009. Measurements of Gas Permeability and Diffusivity of Tight Reservoir Rocks: Different Approaches and Their Applications. *Geofluids* **9** (3): 208–223. https://doi.org/10.1111/j.1468-8123.2009.00244.x.

Curtis, J. B. 2002. Fractured Shale-Gas Systems. *AAPG Bull* **86** (11): 1921–1938. https://doi.org/10.1306/61EEDDBE-173E-11D7-8645000102C1865D.

Dan, Y., Seidle, J. P., and Hanson, W. B. 1993. Gas Sorption on Coal and Measurement of Gas Content. In *Hydrocarbons from Coal*, ed. B. E. Law and D. D. Rice, Vol. 38. Tulsa: AAPG Studies in Geology, American Association of Petroleum Geologists.

Dang, W., Zhang, J.-C., Tang, X. et al. 2017. Investigation of Gas Content of Organic-Rich Shale: A Case Study from Lower Permian Shale in Southern North China Basin, Central China. *Geosci Frontiers* **9** (2): 559–575. https://doi.org/10.1016/j.gsf.2017.05.009.

Darabi, H., Ettehad, A., Javadpour, F. et al. 2012. Gas Flow in Ultra-Tight Shale Strata. *J Fluid Mech* **710** (12): 641–658. https://doi.org/10.1017/jfm.2012.424.

Diamond, W. P., Lascola, J. C., and Hyman, D. M. 1985. Results of Direct-Method Determination of the Gas Content of U. S. Coalbeds. Bureau of Mines Information Circular 9067, US Department of the Interior, Washington, DC.

Ding, X., Mack Kennedy, B., Molins, S. et al. 2017. Experimental Studies and Model Analysis of Noble Gas Fractionation in Low-Permeability Porous Media. *Geochim. Cosmochim. Acta* **205** (15 May): 149–167. https://doi.org/10.1016/j.gca.2017.02.005.

Faiz, M., Zoitsas, A., Altmann, C. et al. 2018. Carbon Isotope Fractionation in Coal and Marine Source Rocks and Implications for Exploration. *Proc.,* AEGC 2018: First Australian Exploration Geoscience Conference, Sydney, 18–21 February, Vol. 1. https://doi.org/10.1071/ASEG2018abP001.

Feng, Z., Liu, D., Huang, S. et al. 2016. Carbon Isotopic Composition of Shale Gas in the Silurian Longmaxi Formation of the Changning Area, Sichuan Basin. *Petrol Explor Develop* **43** (5): 769–777. https://doi.org/10.1016/S1876-3804(16)30092-1.

Golding, S., Boreham, C., and Eserle, J. S. 2013. Stable Isotope Geochemistry of Coalbed and Shale Gas and Related Production Waters: A Review. *Int J Coal Geol* **120** (1): 24–40. https://doi.org/10.1016/j.coal.2013.09.001.

Hu, W., Xue, X., Li, W. et al. 2014. Analysis and Optimization on Determination Method of Gas Content of the Shale. *Sino-Global Energy* **19** (11): 61–66.

Javadpour, F. 2009. Nanopores and Apparent Permeability of Gas Flow in Mudrocks (Shales and Siltstone). *J Can Pet Technol* **48** (8): 16–21. PETSOC-09-08-16-DA. https://doi.org/10.2118/09-08-16-DA.

Jiang, W. and Lin, M. 2017. Molecular Dynamics Investigation of Conversion Methods for Excess Adsorption Amount of Shale Gas. *J Nat Gas Sci Eng* **49** (January): 241–249. https://doi.org/10.1016/j.jngse.2017.11.006.

Krishna, R. 1993. Problems and Pitfalls in the Use of the Fick Formulation for Intraparticle Diffusion. *Chem Eng Sci* **48** (5): 845–861. https://doi.org/10.1016/0009-2509(93)80324-J.

Liu, H., Deng, Z., Liu, D. et al. 2010. Discussion on Lost Gas Calculating Methods in Shale Gas Content Testing. *Oil Drill Product Technol* **32** (S1): 156–158. https://doi.org/10.13639/j.odpt.2010.s1.043.

Meng, Q., Wang, X., Wang, X. et al. 2016. Variation in the Carbon Isotopic Composition of Alkanes During Shale Gas Desorption Process and Its Geological Significance. *J Nat Gas Geosci* **1** (2): 139–146. https://doi.org/10.1016/j.jnggs.2016.05.004.

Naraghi, M. E. and Javadpour, F. 2015. A Stochastic Permeability Model for the Shale-Gas Systems. *Int J Coal Geol* **140** (15 February): 111–124. https://doi.org/10.1016/j.coal.2015.02.004.

Pillalamarry, M., Harpalani, S., and Liu, S. 2011. Gas Diffusion Behavior of Coal and Its Impact on Production from Coalbed Methane Reservoirs. *Int J Coal Geol* **86** (4): 342–348. https://doi.org/10.1016/j.coal.2011.03.007.

Qin, H., Fan, X., Liu, M. et al. 2017. Carbon Isotope Reversal of Desorbed Gas in Longmaxi Shale of Jiaoshiba Area, Sichuan Basin. *Petrol Res* **2** (2): 169–177. https://doi.org/10.1016/j.ptlrs.2016.11.001.

Rahmanian, M. R., Aguilera, R., and Kantzas, A. 2012. A New Unified Diffusion–Viscous-Flow Model Based on Pore-Level Studies of Tight Gas Formations. *SPE J.* **18** (1): 38–49. SPE-149223-PA. https://doi.org/10.2118/149223-PA.

Richter, F. M., Mendybaev, R. A., Christensen, J. N. et al. 2006. Kinetic Isotopic Fractionation During Diffusion of Ionic Species in Water. *Geochim. Cosmochim. Acta* **70** (2): 277–289. https://doi.org/10.1016/j.gca.2005.09.016.

Schloemer, S. and Krooss, B. M. 2004. Molecular Transport of Methane, Ethane and Nitrogen and the Influence of Diffusion on the Chemical and Isotopic Composition of Natural Gas Accumulations. *Geofluids* **4** (1): 81–108. https://doi.org/10.1111/j.1468-8123.2004.00076.x.

Smith, D. M. and Williams, F. L. 1981. A New Technique for Determining the Methane Content of Coal. Oral presentation given at the 16th Intersociety Energy Conversion Engineering Conference, Atlanta, Georgia, 9–14 August.

Smith, D. M. and Williams, F. L. 1984. Diffusion Models for Gas Production from Coals: Application to Methane Content Determination. *Fuel* **63** (2): 251–255. https://doi.org/10.1016/0016-2361(84)90046-2.

Song, W., Yao, J., Li, Y. et al. 2016. Apparent Gas Permeability in an Organic-Rich Shale Reservoir. *Fuel* **181** (1 October): 973–984. https://doi.org/10.1016/j.fuel.2016.05.011.

Urey, H. C. 1947. The Thermodynamic Properties of Isotropic Substances. *Quarterly Journal of the Chemical Society of London*, 562–581.

Weber, A. Z. and Newman, J. 2005. Modeling Gas-Phase Flow in Porous Media. *Int J Heat Mass Transf* **32** (7): 855–860. https://doi.org/10.1016/j.icheatmasstransfer.2004.08.026.

Wei, W., Chao, L., Jian, Z. et al. 2016. Evolution Law and Genesis of Ethane Carbon Isotope of Oil Type Gas. *Acta Petrolei Sinica* **37** (12): 1463–1471. https://doi.org/10.7623/syxb201612002.

Wu, T. and Zhang, D. 2016. Impact of Adsorption on Gas Transport in Nanopores. *Sci Rep* **6**: 23629. https://doi.org/10.1038/srep23629.

Xia, X. and Tang, Y. 2012. Isotope Fractionation of Methane During Natural Gas Flow with Coupled Diffusion and Adsorption/Desorption. *Geochim. Cosmochim. Acta* **77** (1): 489–503. https://doi.org/10.1016/j.gca.2011.10.014.

Yao, G., Wang, X., Du, H. et al. 2016. Applicability of USBM Method in the Test on Shale Gas Content. *Acta Petrolei Sinica* **37** (6): 802–806. https://doi.org/10.7623/syxb201606011.

Yi, J., Akkutlu, I. Y., Karacan, C. Ö. et al. 2009. Gas Sorption and Transport in Coals: A Poroelastic Medium Approach. *Int J Coal Geol* **77** (1–2): 137–144. https://doi.org/10.1016/j.coal.2008.09.016.

Ying, T., Zhang, J., Liu, Z. et al. 2011. Use and Improvement of the Desorption Method in Shale Gas Content Tests. *Nat Gas Industry* **31** (10): 108–112.

Yuan, W., Pan, Z., Li, X. et al. 2014. Experimental Study and Modelling of Methane Adsorption and Diffusion in Shale. *Fuel* **117A** (30 January): 509–519. https://doi.org/10.1016/j.fuel.2013.09.046.

Zhang, J., Jin, Z., and Yuan, M. 2004. Reservoiring Mechanism of Shale Gas and Its Distribution. *Nat Gas Industry* **24** (7): 15–18.

Zhang, J., Lin, L. M., Li, Y. X. et al. 2012. The Method of Shale Gas Assessment: Probability Volume Method. *Earth Sci Frontiers* **19** (2): 184–191.

Zhang, M., Tang, Q., Cao, C. et al. 2018. Molecular and Carbon Isotopic Variation in 3.5 Years Shale Gas Production from Longmaxi Formation in Sichuan Basin, China. *Mar Pet Geol* **89** (January): 27–37. https://doi.org/10.1016/j.marpetgeo.2017.01.023.

Zhang, T. and Krooss, B. M. 2001. Experimental Investigation on the Carbon Isotope Fractionation of Methane During Gas Migration by Diffusion Through Sedimentary Rocks at Elevated Temperature and Pressure. *Geochim. Cosmochim. Acta* **65** (16): 2723–2742. https://doi.org/10.1016/S0016-7037(01)00601-9.

Appendix A—Flow Flux in a Bundle of Capillary Tubes

Assuming the flow channel consists of a series of pores, we consider gas transport in the bundle of capillary tubes. The pore with the radius of r_j occupies the flow porosity of $\phi_{f,j}$. The total flow flux is calculated as

$$N_i = -\sum_j \frac{\nabla p_i}{RT} \frac{\phi_{f,j}}{\tau} \left(\frac{2r_j}{3} \sqrt{\frac{8RT}{\pi M_i}} + \frac{p r_j^2}{8\mu} \right). \quad\dots\dots\dots\dots\dots\dots\dots\dots\dots\dots\dots\dots\dots\dots\dots\dots \text{(A-1)}$$

To obtain the flow porosity of each pore, when knowing the volumetric faction α_j for the pore r_j and the total flowing porosity, $\phi_{f,j}$ can be expressed as

$$\phi_{f,j} = \phi_f \alpha_j \quad\dots\dots\dots\dots\dots\dots\dots\dots\dots\dots\dots\dots\dots\dots\dots\dots\dots\dots\dots\dots\dots\dots\dots\dots \text{(A-2)}$$

α_j can be obtained from the pore-size distribution measured by the nitrogen-adsorption experiment.

Gaohui Cao is a PhD-degree candidate at the Institute of Mechanics, Chinese Academy of Sciences. His research is focused on fluid mechanics, trans-scale simulation, fractionation, and shale-gas exploration. Cao has authored or coauthored more than six technical papers related to those topics. He holds a bachelor's degree in hydraulic engineering from Tsinghua University, China.

Huanxu Zhang holds a post-doctoral-degree position at the College of Engineering, Peking University, China. His research interests are hydrocarbon accumulation, reservoir geochemistry, and shale-gas exploration. Zhang holds a bachelor's degree in geophysics from Yangtze University, China, and master's and PhD degrees in geochemistry from Southwest Petroleum University, China.

Wenbin Jiang is an associate professor at the Institute of Mechanics, Chinese Academy of Sciences. His research interests include flow mechanisms in shale-gas production and the rebuilding and scaleup of pore space in unconventional reservoirs. Jiang holds a bachelor's degree from Tsinghua University and a PhD degree from the Institute of Mechanics, Chinese Academy of Sciences.

Sheng Wu is the research lead for sensors, tight oil, and gas-production geology at the Power Environmental Energy Research Institute. The sensors and techniques developed are applied to petroleum drilling and refinery engineering and biological science. Wu developed a wellsite compound-specific isotope analyzer and contributed to the discovery of the Merge tight oil and gas field in Oklahoma. He holds bachelor's degrees in chemistry and physics from Peking University and master's and PhD degrees from the California Institute of Technology.

Di Zhu is a senior researcher at the Energy Research Institute, Qilu University of Technology (Shandong Academy of Science), China. His work ranges from instrumental analysis to geochemistry study. Together with other researchers, Zhu developed a carbon-isotope analyzer and novel quantitative methods toward investigating the gas content of organic-rich shale. He holds a bachelor's degree from Peking University and a PhD degree from the University of Wisconsin, Madison.

Mian Lin is a professor of fluid mechanics at the Institute of Mechanics, Chinese Academy of Sciences. Her main interests include flow mechanisms in shale-gas exploration and production and the rebuilding and scaleup of pore space in unconventional reservoirs. Lin has authored or coauthored more than 20 papers on related topics.